Materials Science & Engineering A 576 (2013) 167–177

Contents lists available at SciVerse ScienceDirect

Materials Science & Engineering A

journal homepage: www.elsevier.com/locate/msea

The effect of cooling rates on the microstructure and mechanical properties of thermo-mechanically processed Ti–Al–Mo–V–Cr–Fe alloys

Mansur Ahmed [a,*], Dmytro G. Savvakin [b], Orest M. Ivasishin [b], Elena V. Pereloma [a,c]

[a] School of Mechanical, Materials and Mechatronic Engineering, University of Wollongong, NSW 2522, Australia
[b] Institute for Metal Physics, National Academy of Sciences of Ukraine, UA-03142 Kiev, Ukraine
[c] Electron Microscopy Centre, University of Wollongong, NSW 2519, Australia

ARTICLE INFO

Article history:
Received 7 November 2012
Received in revised form
15 March 2013
Accepted 29 March 2013
Available online 11 April 2013

Keywords:
Ti alloys
Cooling rate
X-ray diffraction
Microstructure
Mechanical properties

ABSTRACT

Two near-β titanium alloys, Ti–5Al–5Mo–5V–1Cr–1Fe and a modified one containing 2 wt% Cr (Ti–5Al–5Mo–5V–2Cr–1Fe) were produced from Ti hydride precursor powders via the cost-effective blended elemental powder metallurgy technique. The effects of two cooling rates (10 K s^{-1} and 1 K s^{-1}) during thermo-mechanical processing on the microstructure and mechanical properties were investigated using X-ray diffraction and scanning electron microscopy. X-ray line profile analysis revealed that dislocation densities and microstrain in β-Ti phase are higher than in α-Ti phase for all cases. In both alloys, slower cooling results in an increase in α volume fraction and promotes morphology of continuous grain boundary α phase. A lower total elongation is obtained in both alloys under slower cooling which could be accounted for by the continuous morphology of α phase. Overall, Ti–5Al–5Mo–5V–1Cr–1Fe displays higher ultimate tensile strength and total elongation compared to Ti–5Al–5Mo–5V–2Cr–1Fe, regardless of the cooling rate.

1. Introduction

Ti based alloys are used in the aerospace, automotive and medical industries due to their attractive properties, particularly high strength-to-density ratios [1–3]. Extensive research has been carried out in order to reduce the production costs, particularly over the last decade [4–6]. One of the most promising cost-effective powder metallurgical techniques is the blended elemental powder metallurgy (BEPM) method [7]. A number of Ti based alloys [7–12] have been produced using powder metallurgy technique where an additional processing step called the hot isostatic pressing (HIP) is used in order to increase relative density or reduce the residual porosity. This results in an extra processing cost which compromises the cost savings of powder metallurgy technique. Ye et al. [13] have thereafter used uniaxial hot pressing at much lower pressure (~15 MPa for Ti64) than HIP (~150 MPa for Ti64) in the α/β phase transformation range in order to replace the HIP. This approach has reduced processing cost compared to the HIP but it still remains expensive. Later on, only the press-and-sinter method has been employed in [14–18] which unfortunately produced the density close to ~90% only. Finally, Ti hydride powder is used with BEPM technique without HIP. In this method a uniform network of fines pores, which form during cold compaction of brittle TiH_2 powder particles, are healed upon sintering. Due to $TiH_2 \rightarrow Ti+2H$ phase transformation high density of crystal lattice defects evolve which accelerates the synthesis. The evolution of atomic hydrogen promotes mass transfer through the inter-particle boundaries which reduces surface oxides/residual porosity. The obtained sintered density was close to ~99% by using Ti powders containing 3 wt% hydrogen [19]. This is considered to be the lowest cost powder metallurgy technique. The studied alloys have been produced using this methodology. Near-β Ti alloys are used in the aerospace industries particularly due to their deep hardenability, high strength and creep properties. A near-β Ti alloy consists typically of two phases: hard α phase and soft β phase. Several investigations have been carried out on the effect of the thermal processing on the microstructure and mechanical properties. In [4,20,21], the influence of α phase morphology on the mechanical properties has been analysed. It is reported in [20,21] that globular shaped α phase has positive effect on the mechanical properties, especially on ductility.

X-ray diffraction line profile analysis (XRDLPA) and transmission electron microscopy (TEM) are used to determine the crystallite dimensions, lattice microstrain and dislocation densities of the submicron grains in the microstructure. The results obtained through TEM analysis are locally accurate but may not be representative of the bulk material. In contrast, XRDLPA involves significantly larger sample volumes and is useful provided that the volume fractions of relevant phases are high enough to result in clear XRD peaks for analysis. For materials containing two or

* Corresponding author. Tel.: +61 2 4221 5798; fax: +61 2 4221 3662.
E-mail address: ma960@uowmail.edu.au (M. Ahmed).

0921-5093/$ - see front matter © 2013 Elsevier B.V. All rights reserved.
http://dx.doi.org/10.1016/j.msea.2013.03.083

more phases, it generally is more convenient to use XRD as the peaks of the constituent phases appear distinctly in the profile. Several XRDLPA investigations have been performed on steels [22–26], Cu [27–29] and Zr [30,31] alloys. In contrast, a fewer number of investigations using the XRDLPA have been performed on Ti alloys [32–34]. Glavicic et al. [32] have used X-ray line profile analysis to examine the slip activity in commercially pure Ti. Later on, they have measured dislocation densities for individual α and β phases in Ti–6Al–4V alloy [33]. Deformed microstructures of boron doped Ti–6Al–4V alloys have been characterised in terms of crystallite size and dislocation density using variance and the modified Rietveld method [34] with findings that the dislocation densities are higher in β phase than in α phase [22,23].

In the present study, two near-β titanium alloys, Ti–5Al–5Mo–5V–1Cr–1Fe (Ti-55511) and a variant containing 2 wt% Cr (Ti-55521) were produced via the BEPM technique using Ti hydride powder. The Ti-55511 alloy is selected because of its use in aerospace industries [35] and this is the first attempt for this alloy production using cost-effective BEPM technique. A novel Ti-55521 alloy is chosen because increased Cr contents reduce the amount of α phase [36,37] during soaking in α+β phase field potentially results in improvements in ductility [21]. The aim of the present work is to characterise the microstructure and mechanical properties of the alloys subjected to the thermo-mechanical processing (TMP). In particular, the effects of Cr addition and two cooling rates are investigated.

2. Experimental and analysis methods

2.1. Materials

Hydrogenated (3.5 wt% H) Ti powders were mixed with elemental Mo, Cr, Fe (<40 μm) and Al–V master alloy powders (40–63 μm) in order to obtain the required alloy composition. The powders were blended and die pressed under 650 MPa to form green compacts. The green compacts were thereafter sintered by heating to 1293 K for 3600 s followed by heating to 1523 K for 21,600 s in order to distribute the alloying elements throughout the matrix uniformly. The results obtained after sintering have shown in [38] that all the alloying elements distributed homogeneously throughout the matrix after sintering step II (1523 K for 21,600 s). The sintered compacts were provided by Institute for Metal Physics, National Academy of Sciences, Ukraine. Thereafter, a Gleeble 3500 thermo-mechanical simulator with modest vacuum ($\sim 3.8 \times 10^{-4}$ Torr) in pocket jaw mode was employed for the TMP.

The TMP schedule is shown in Fig. 1 and involved the heating of cylindrical samples (12 mm length × 8 mm diameter) to 1223 K at 10 K s^{-1} and holding for 120 s, then cooling at 35 K s^{-1} to 1173 K where a 25% length reduction takes place. This is followed by cooling at 35 K s^{-1} to 1073 K where after the hold for 1800 s a deformation to 60% reduction is applied. After deformation, the samples are given a final cool to room temperature at either of the two selected cooling rates; 10 K s^{-1} or 1 K s^{-1}. The samples are cut perpendicular to the deformation direction and prepared using conventional metallographic techniques. The polished samples are etched using Kroll's reagent (2 ml HF, 5 ml HNO_3 and 93 ml H_2O) in order to reveal the microstructure.

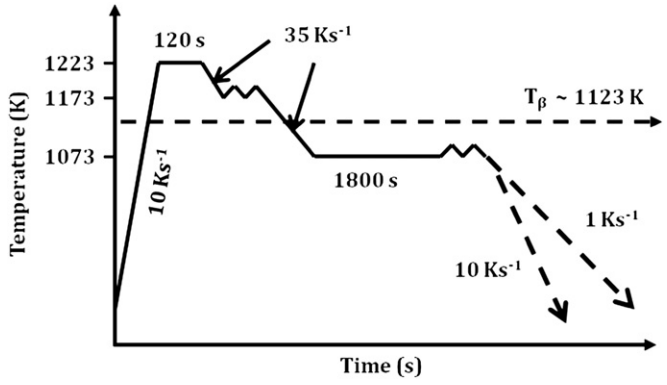

Fig. 1. A schematic diagram of the thermo-mechanical processing schedules.

2.2. X-ray data acquisition

X-ray diffraction investigations were conducted using a PANalytical X'Pert PRO Multipurpose diffractometer (MPD) with Cu Kα radiation ($\lambda = 0.154$ nm) filtered with Ni-monochromator at 45 mA and 40 kV. Polished samples of diameter 15 mm were oriented normal to the deformation axis. Diffraction patterns were obtained under a continuous scanning mode over the 2θ range of 30–160°, with 0.01° step size and 490 s resulting acquisition time. In order to characterise the instrumental broadening a standard polycrystalline silicon sample was used.

2.2.1. Method of X-ray diffraction line profile analysis

Diffraction from a crystalline material provides information about both periodic and internal crystalline features. In the diffraction pattern such information can be inferred from calculations related to peak position, peak shape and peak width. Broadening of the peaks can occur due to a decrease in crystallite size, and/or due to microstrain within the crystallite. The width of the diffraction peaks also depends on the instrumental factors. Other factors such as dislocation density, slip activity [32], and the presence of stacking faults can also affect the shape and/or position of diffraction peaks [27]. Warren [39], Randle and Engler [40] developed the XRDLPA approach for the analysis of the microstructure, which was later followed by others [28,41–45] with some modifications making it possible to determine the crystallite size and microstrain in materials reliably. Similarly to [16,23], the modified Rietveld [46] method has been used in order to characterise microstructures in this investigation. The brief algorithms of the modified Rietveld method used are presented below.

2.2.1.1. The modified Rietveld method. The modified Rietveld method consists of a modelling of diffraction profiles through pseudo-Voigt (pV) function using the programme LS1 [46]. The crystal structure of the materials and microstructural parameters, e.g. lattice parameters, crystallite size and microstrain, are simultaneously refined through the LS1 programme. In the programme, Fourier transform of the pV function is used to fit the broadening of the peaks profile. An isotropic model is assumed, which is called the Popa model [47] where the lattice constants, volume weighted crystallite size and microstrain are concomitantly used as the fitting parameters. Since the samples are heavily deformed, the preferred orientation of the crystallites has been corrected in order to obtain the best fit by maintaining the following function, $P(\alpha)$ [48]:

$$P(\alpha) = (r^2 \cos^2\alpha + r^{-1}\sin^2\alpha)^{-3/2} \quad (1)$$

Here, α is the angle between the preferred orientation vector and the normal to the planes generating the diffracted peak and r is a refinable parameter. In all conditions, the diffraction profiles were fitted up to 100° (2θ) using the above mentioned approach because of the very low intensity of the peaks above 100°.

The Goodness of fit (*GoF*) indicates the quality of the fitting which is expressed as follows:

$$GoF = R_{wp}/R_{exp} \tag{2}$$

Here, R_{wp} is the weighted residual profile and R_{exp} is the expected profile.

2.2.1.2. The calculation of dislocation density and stored energy. The amount of dislocation density depends on the value of crystallite size and microstrain of crystallographic planes peaks. The value of dislocation density, $\langle p\rangle$, is thereafter calculated using the following equation obtained from [49]

$$\langle\rho\rangle = \frac{3\sqrt{(2\pi)}\langle\in_L^2\rangle^{1/2}}{D_s b}. \tag{3}$$

Here, D_s is the crystallite size, $\langle\in_L^2\rangle^{1/2}$ is the microstrain and b is Burger's vector. Burger's vector for hexagonal closed packed planes (b_{hcp}) and for body-centered cubic planes (b_{bcc}) is

b_{hcp} = lattice parameter of basal plane (a) which is 0.293 nm in the present study; (3.1)

$$b_{bcc} = \frac{\text{lattice parameter}}{2}\left|\langle hkl\rangle\right| \tag{3.2}$$

Finally, stored energy (E_s) due to the inhomogeneous microstrain is calculated using the Stibitz relationship [50]:

$$E_s = 1.5Y\frac{(\Delta d/d)^2}{1+2\upsilon^2}. \tag{4}$$

Here, Y is Young's modulus of the material. The value of Y is equal to 116 GPa [51] for hcp-Ti and 68 GPa [52] for bcc-Ti. The value of Poisson's ratio (ν) is equal to 0.32 for hcp-Ti [53] and 0.23 for bcc-Ti [54]. The value of stored energy (E_s) is expressed in J mol^{-1} assuming the molar volume 10.46 cm^3 mol^{-1}. The relative change in lattice spacing ($\Delta d/d$) is derived from the broadening of the peak [55]:

$$(\Delta d/d) = w/2\tan\theta \tag{4.1}$$

Here, w is the broadening of the peaks and θ is the half of the Bragg angle (2θ) corresponding to the peak.

2.3. Microstructure and mechanical properties

A JEOL-JSM 7001F Field Emission Gun-Scanning Electron Microscope (FEG-SEM) was used to investigate the microstructures of the samples. Operating at 15 kV and 15 mm working distance both the back scattered electron and secondary electron modes were employed for imaging. TMP samples were machined into sub-sized tensile specimens (Fig. 2) of gauge length 5.1 mm; width 2.18 mm and thickness 0.9 mm. Tensile tests were carried out with a μ-Tweezer Tensile Module (Kammrath & Weiss, GmbH) at a constant speed of 1.7 mm min^{-1} at room temperature. In order to understand the work hardening behaviour of the samples and to find the m-values (work hardening exponent) of different stages of the plastic regions in the stress–strain curves of the samples, stress–strain curves were fitted using rational polynomial functions via 2D-TableCurve.

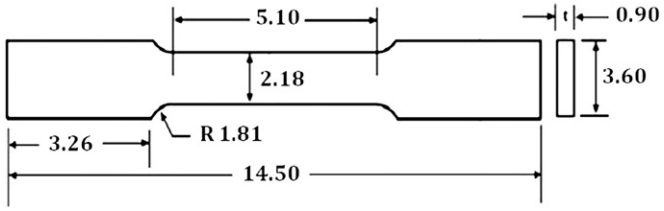

Fig. 2. A schematic of the tensile specimens (two dimensional) with dimensions. All dimensions are in mm.

Table 1
The values of agreement indices of the Rietveld fitting for the alloys at different cooling conditions.

Alloy	Cooling rate (K s^{-1})	Residual weighed profile (R_{wp}), %	Goodness of fit (*GoF*)
Ti-55511	10	9.1	1.6
	1	8.8	0.9
Ti-55521	10	7.4	1.0
	1	7.9	0.9

3. Results

3.1. X-ray line profile analysis and phase transformation

A summary of agreement indices of the Rietveld fitting for all samples is shown in Table 1. The obtained value of residual weighted profile (R_{wp}) is in between 7.4% and 9.1% as well as Goodness of fit (*GoF*) is lying between 0.9 and 1.6. Fig. 3 indicates X-ray diffraction patterns and associated Rietveld fitting for all samples where peaks from α and β phases with *Miller–Bravais* indices are clearly exhibited. The intensity difference between the experimental and the Rietveld fitting is also plotted under the diffraction patterns. The trend of the X-ray diffraction patterns is similar for the samples cooled at the same rate for both alloys. For both alloys, there is an obvious reduction in β planes peaks intensities for the samples cooled at 1 K s^{-1} compared to those for the samples cooled at 10 K s^{-1}. On the other hand, α planes peaks intensities show opposite character to β planes peaks. The 2θ position of all β planes peaks shifts slightly to the right in the diffraction profiles compared to those of the pure unalloyed β-Ti.[1] The similar results indicating the shift of β planes peaks to the right have been found in other Ti alloys, e.g. Ti–25V–15Cr–0.2Si [56] and Ti–30Zr–5Al–3V [57].

Tables 2 and 3 are the summary of the Rietveld analyses, indicating values of lattice parameter, crystallite size and microstrain of the several α and β planes, respectively. Dislocation density and stored energy values is calculated using Eqs. (3) and (4) and also included in Tables 2 and 3. In Table 2, only basal lattice parameter (a) of hcp lattice is given because prism lattice parameter (c) could easily be obtained from the c/a ratio. The c/a ratio of hcp lattices has been calculated using the following equation [58]:

$$\frac{c}{a} = \frac{\sqrt{3}}{2}\frac{\sin\theta_{(h0\bar{h}0)}}{\sin\theta_{(000l)}}\frac{l}{h} \tag{5}$$

Here, $\sin\theta_{(h0\bar{h}0)}$ is equal to $\sin\theta_{(10\bar{1}0)}$ and $\sin\theta_{(000l)}$is equal to $\sin\theta_{(0001)}$ in the present study. By using Eq. (5), the c/a ratio (~1.6) is calculated for all samples which are similar to those for an unalloyed α-Ti. Thus, it may be claimed that alloying and cooling rates did not influence the c/a ratio of hcp lattices. On the other hand, the average of the β-Ti lattice parameter is 0.3235 nm for both alloys, which is slightly less than that for the unalloyed β-Ti

[1] PDF Reference Code: 03-065-5970.

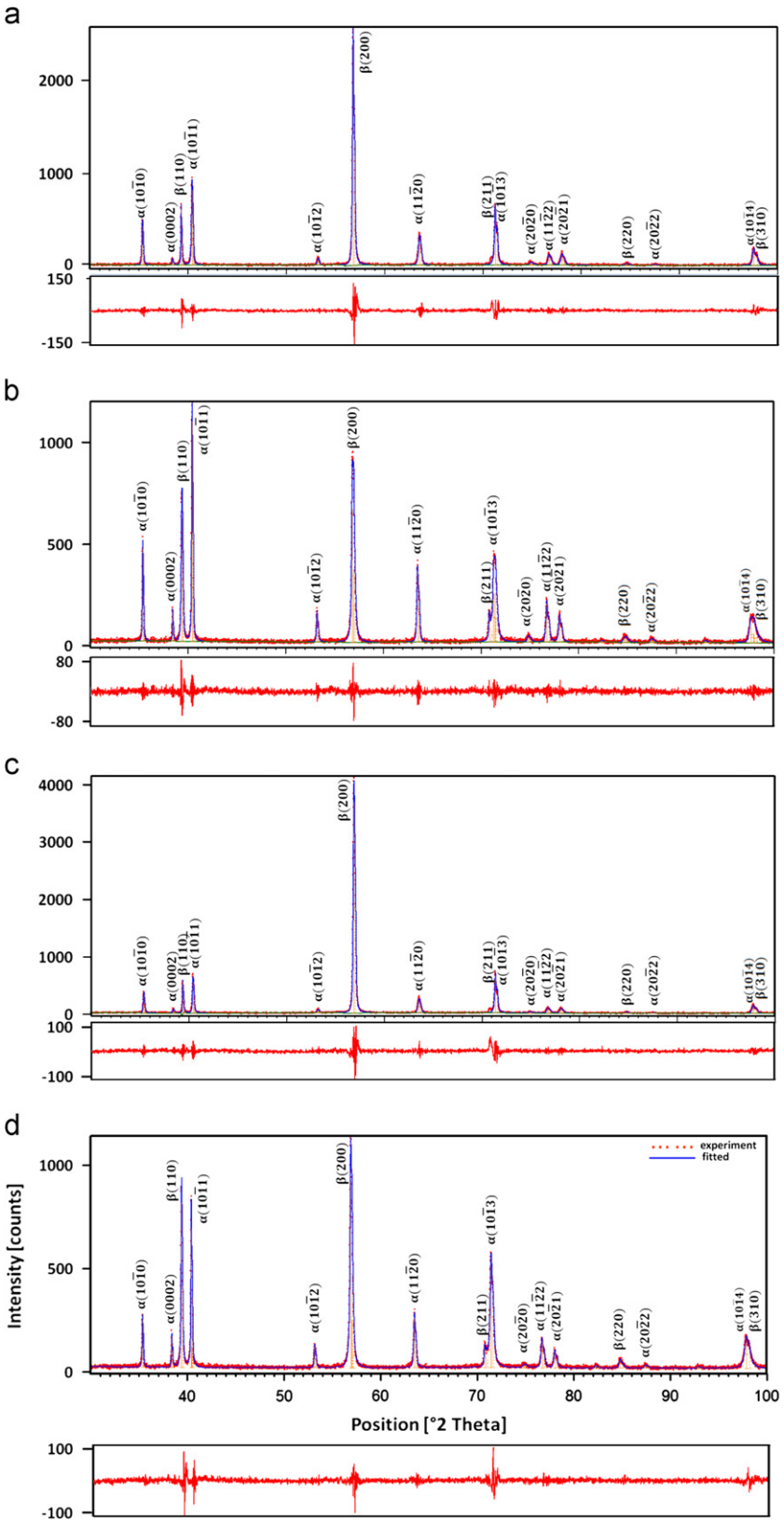

Fig. 3. X-ray diffraction patterns and Rietveld fitting of (a and b) Ti-55511 and (c and d) Ti-55521 alloys cooled at 10 K s^{-1} (a and c) and 1 K s^{-1} (b and d), respectively. Difference between the experiment and Rietveld fitting is shown below each pattern.

(0.3311 nm). For both alloys, a slightly larger reduction in the bcc lattice parameter is obtained for slow cooling rate (1 K s^{-1}). On the other hand, the Ti-55521 alloy has slightly smaller bcc lattice parameter than Ti-55511 alloy.

In this study, the dominant lattice planes α(10$\bar{1}$0), α(0002), α(10$\bar{1}$1), α(10$\bar{1}$2), and α(11$\bar{2}$0) in the diffraction profiles are analysed. In both alloys, the crystallite size of α planes peaks is found to be higher for the samples cooled at 1 K s^{-1} compared to

Table 2
The values of lattice parameters (a and c *), crystallite size (D_s), microstrain $(\langle\varepsilon_L^2\rangle)^{1/2}$, dislocation density $\langle p\rangle$ and local stored energy (E_s) obtained from the Rietveld analysis and other formula for several α planes.

Miller indices	Alloy	Cooling rate (K s^{-1})	a (nm)	D_s (nm)	$(\langle\varepsilon_L^2\rangle)^{1/2}$ ($\times 10^{-4}$)	$\langle p\rangle \pm 0.02$max ($\times 10^{14}$ m^{-2})	E_s (J mol^{-1})
$(10\bar{1}0)$	Ti-55511	10	0.293	165 ± 9	10.5	1.65	3.4
		1	0.293	219 ± 12	7.9	0.94	1.9
	Ti-55521	10	0.293	135 ± 5	11.2	2.15	3.9
		1	0.293	175 ± 7	8.4	1.24	2.2
(0002)	Ti-55511	10	0.293	111 ± 6	7.7	1.80	1.8
		1	0.293	371 ± 13	5.5	0.38	0.95
	Ti-55521	10	0.293	88 ± 3	9.1	2.68	2.6
		1	0.293	197 ± 8	6.1	0.80	1.2
$(10\bar{1}1)$	Ti-55511	10	0.293	192 ± 6	10.3	1.39	3.3
		1	0.293	234 ± 17	7.4	0.82	1.7
	Ti-55521	10	0.293	178 ± 3	10.7	1.56	3.5
		1	0.293	198 ± 11	8.1	1.06	2.0
$(10\bar{1}2)$	Ti-55511	10	0.293	181 ± 12	14.3	2.05	6.3
		1	0.293	211 ± 5	6.2	0.76	1.2
	Ti-55521	10	0.293	97 ± 7	19.7	5.26	11.8
		1	0.293	206 ± 8	8.9	1.12	2.5
$(10\bar{2}0)$	Ti-55511	10	0.293	134 ± 10	15.2	2.94	7.1
		1	0.293	193 ± 2	9.2	1.24	2.6
	Ti-55521	10	0.293	117 ± 8	17.3	3.83	9.2
		1	0.293	146 ± 6	10.6	1.88	3.4

* Lattice parameter, $c = 1.6 \times a$ (for hcp).

Table 3
The values of lattice parameter (a), crystallite size (D_s), microstrain $(\langle\varepsilon_L^2\rangle)^{1/2}$, dislocation density $\langle p\rangle$ and local stored energy (E_s) obtained from the Rietveld analysis and other formula for several β planes.

Miller indices	Alloy	Cooling rate (K s^{-1})	a (nm)	D_s (nm)	$(\langle\varepsilon_L^2\rangle)^{1/2}$ ($\times 10^{-4}$)	$\langle p\rangle \pm 0.05$ ($\times 10^{14}$ m^{-2})	E_s (J mol^{-1})
(110)	Ti-55511	10	0.3238	143 ± 5	11.4	2.61	2.3
		1	0.3233	92 ± 9	18.8	6.68	6.3
	Ti-55521	10	0.3233	179 ± 3	9.6	1.75	1.6
		1	0.3230	108 ± 14	16.3	4.93	4.8
(200)	Ti-55511	10	0.3238	147 ± 12	9.9	1.56	1.7
		1	0.3234	79 ± 6	13.6	4.00	3.3
	Ti-55521	10	0.3234	187 ± 9	8.4	1.04	1.3
		1	0.3230	102 ± 10	12.9	2.94	2.9
(310)	Ti-55511	10	0.3238	82 ± 7	11.1	1.99	2.2
		1	0.3232	28 ± 6	13.5	7.09	3.7
	Ti-55521	10	0.3233	68 ± 5	16.8	3.64	5.0
		1	0.3231	46 ± 8	18.3	5.85	6.8

that for the samples cooled at 10 K s^{-1}. This is accompanied by the reduction in crystallite microstrain after slower cooling. Thus, dislocation density and local stored energy in the α lattice planes is lower for both alloys cooled at 1 K s^{-1} compared to those cooled at 10 K s^{-1}. On the other hand, α crystallite size of the Ti-55521 alloy is always smaller and the microstrain is larger than those for the Ti-55511 alloy under the respective cooling condition. As a result, the dislocation density and stored energy are found to be higher in the Ti-55521 compared to Ti-55511 alloy under the respective cooling rate. In the case of β peaks, β (110), β (200), and β (310) lattice planes are analysed. Despite of the good intensity, β (211) plane is not analysed as it overlaps with α$(10\bar{1}3)$ peak. In both alloys, the crystallite size of β planes peaks decreases for the samples cooled at 1 K s^{-1} compared to the samples cooled at 10 K s^{-1}. There is an increase in microstrain of β crystallite of the samples cooled at 1 K s^{-1}. Consequently, the dislocation density and local stored energy of the β planes are found to be higher for both alloys cooled at 1 K s^{-1}. However, after similar processing the β crystallite size is larger for the Ti-55521 alloy compared to the Ti-55511 alloy. Dislocation density and stored energy are found to be a bit higher for the Ti-55521 alloy. Overall, the dislocation densities and microstrain in β planes peaks are higher than those in α planes peaks.

3.2. Microstructural development

Fig. 4 represents the microstructures of both alloys for all cooling conditions. The microstructures consist of both α and β phases with α phase displaying different morphologies: lamellar shape and globular shape. The lamellar shape α can later form basket weave structure if they lie in different planes, as can be seen in Fig. 4f in the areas denoted by circles. Within the basket weave structure in Fig. 4f, there are also visible arrangements of triangular-shaped α consisting of three interconnected α lamellae. There are also some parallel α lamellae arrangements, indicated by a rectangular box in Fig. 4f. In both alloys, recrystallised β grains are visible in the microstructures under both cooling conditions, but it is more pronounced after slower cooling. In the case of both

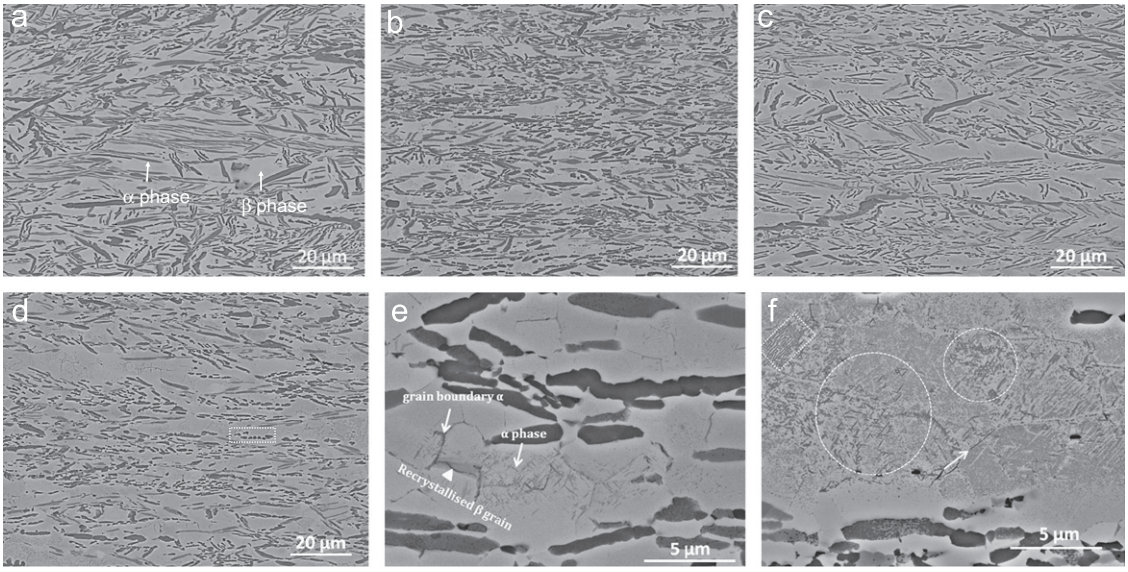

Fig. 4. The microstructures of the alloys showing α and β phases. (a) Ti-55511 alloy cooled at 10 K s^{-1}, (b) Ti-55511 alloy cooled at 1 K s^{-1}, (c) Ti-55521 alloy cooled at 10 K s^{-1}, and (d) Ti-55521 alloy cooled at 1 K s^{-1}. (e) Enlarged view of Ti-55521 alloy cooled at 1 K s^{-1} showing interconnected grain boundary α phase. (f) Initiation of the grain boundary α phase formation (arrow marked) and triangular shaped α phase (circle marked)—in Ti-55511 alloy. Parallel lamellar α in the top left corner (indicated by rectangular box).

alloys cooled at 1 K s^{-1}, the microstructures also reveal a continuous network of grain boundary α formed at the β grain boundaries. In addition, there are fine α lamellae lying inside the recrystallised β grains which also form a basket weave structure. Microstructural observations, such as those shown in Fig. 5 (indicated by a rectangular areas and an arrow), reveal that the α phase formation first takes place at the interface of the β phase crystals, and with time, the remaining β phase surrounded by the newly formed α, transforms into the α phase.

The porosity of the alloys is reduced from ~2% after sintering to ~0.10% after TMP [38]. Table 4 indicates that the amount of α phase varies with the alloy composition and cooling rates. A maximum volume fraction of α phase of 54 ± 2% is obtained in the case of Ti-55511 alloy cooled at 1 K s^{-1}, whereas the minimum amount of α phase (34 ± 3%) is obtained in the case of Ti-55521 alloy cooled at 10 K s^{-1}. Regardless of the cooling rate, Ti-55521 alloy contains a lesser amount of α phase compared to Ti-55511 alloy. On the other hand, both alloys show a higher amount of α phase for the samples cooled at 1 K s^{-1} compared to those cooled at 10 K s^{-1}.

3.3. Mechanical properties

Fig. 6 shows the engineering stress versus strain curves of both alloys for all cooling conditions. The shape of these curves is quite similar for all samples. A summary of the mechanical properties based on Fig. 6 is also given in Table 4. A maximum ultimate tensile strength (UTS) of 1189 ± 7 MPa is obtained in the case of Ti-55511 alloy cooled at 1 K s^{-1}, whereas a maximum total elongation of 9.85 ± 0.05% is obtained in the case of Ti-55511 alloy cooled at 10 K s^{-1}. For the same cooling conditions, Ti-55511 alloy displays a higher UTS compared to Ti-55521 alloy. On the other hand, specimens subjected to 10 Ks^{-1} cooling rate show lower UTS values compared to those cooled at 1 K s^{-1}. Table 5 shows Vickers micro-hardness values for α and β phases from which 0.2% offset yield strength of the samples is calculated using the rule of mixtures.[2] Table 5 also clearly indicates that estimated 0.2% offset yield strength correlates well with the experimental data.

[2] Rule of mixtures, Total strength = vol. fraction of phase 1 × strength of phase 1+vol. fraction of phase 2 × strength of phase 2.

The work hardening behaviour is analysed using the modified Crussard–Jaoul (C–J) model [59–63], as the samples contain two phases similar to dual phase steel for which this model was developed. The modified C–J model uses the following Eq. (6) which is known as the Swift equation [59]:

$$\varepsilon = \varepsilon_0 + C_s\sigma^m \tag{6}$$

Here, σ is the true stress, ε is the true strain, m is the work hardening exponent and C_s is the material constant. The logarithmic form of the differential Swift equation with respect to ε gives the following:

$$\ln(d\sigma/d\varepsilon) = (1-m)\ln\sigma - \ln(C_s m) \tag{7}$$

It can be seen that Eq. (7) represents the linear relation between logarithmic form of work hardening rate, $\ln(d\sigma/d\varepsilon)$, and logarithmic form of true stress, $\ln\sigma$, where $(1-m)$ is the slope of the line. The logarithm of work hardening rate, $\ln(d\sigma/d\varepsilon)$, versus logarithm of true stress, $\ln\sigma$, is plotted for all the samples in Fig. 7a. The trend of the curves for all samples is quite similar. Each of the curves is segmented into three distinct stages as per depicted in Fig. 7b (stage I, stage II and stage III), with a maximum slope in stage II and a minimum one in stage III. A summary of the results obtained from Fig. 7a is presented in Table 6, where the work hardening exponent (m) values corresponding to each stage are given together with the transition true stress and true strain values. The maximum value of the work hardening exponent is obtained for stage II (m_{II}) and the minimum work hardening exponent is obtained for stage III (m_{III}) in all the samples. Regardless of cooling conditions, the values of transition strain from stage I to stage II and stage II to stage III are slightly higher for the Ti-55511 alloy compared to the Ti-55521 alloy.

4. Discussion

4.1. X-ray line profile analysis and phase transformation

The effect of slower cooling (1 K s^{-1}) on the β to α phase transformation can easily be understood from the diffraction profiles. A reduction in relative intensities of the β peaks and an increase in relative intensities of the α peaks for the samples

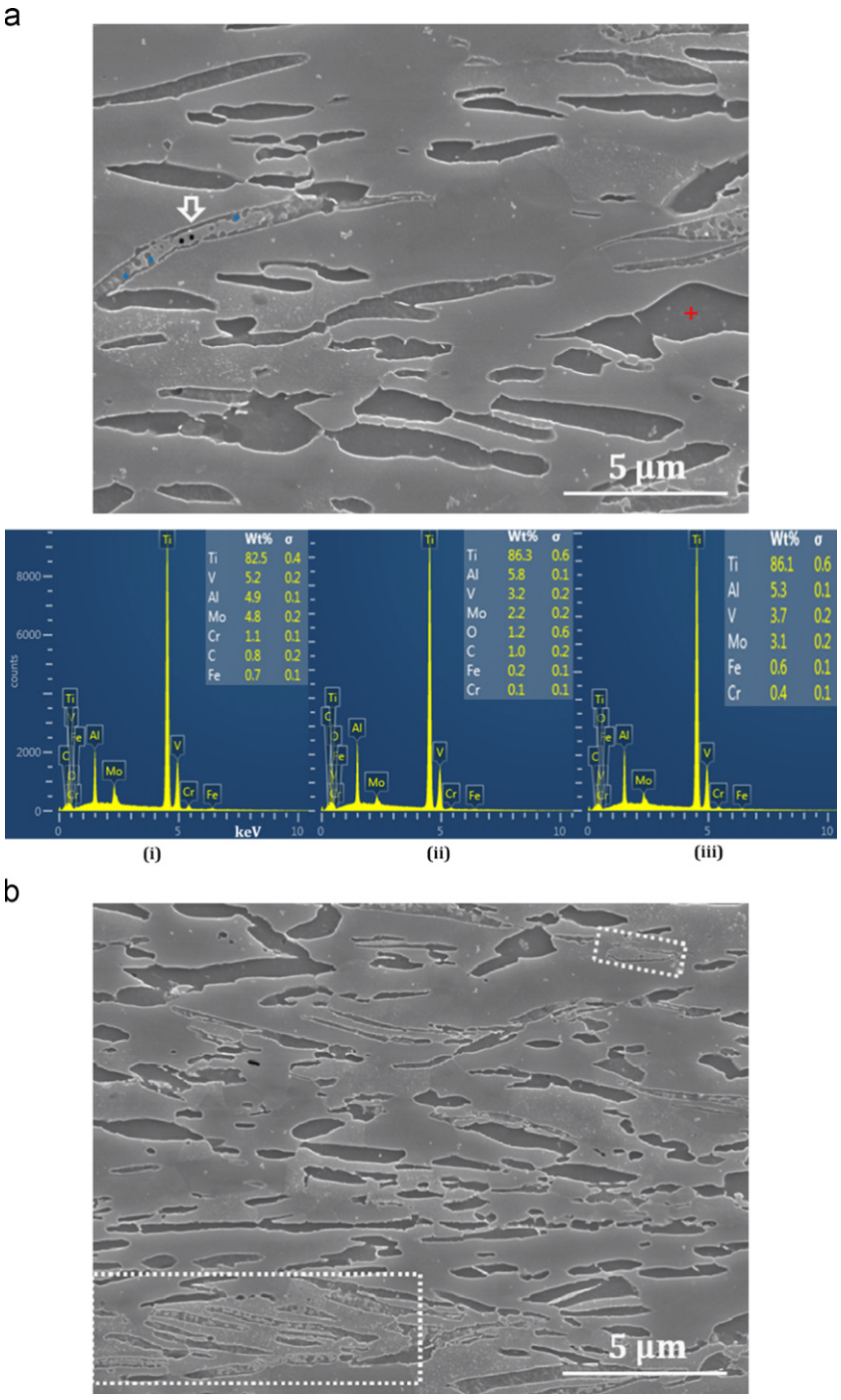

Fig. 5. The examples of different morphologies of α and β phases with corresponding EDX profiles indicating the progress of β→α transformation. The arrow head in (a) and rectangular boxes in (b) indicate the fields of interest in the microstructure. For (a): (i) the composition of untransformed β corresponds to the "black dot" in the region indicated by an arrow; (ii) the composition of transformed α corresponds to the "blue dot" in the same region, and (iii) the composition of α phase taken from the area identified by "+" in (a). (For interpretation of the references to colour in this figure legend, the reader is referred to the web version of this article.)

Table 4
The volume fractions of α phase (V_α), 0.2% offset yield strength (σ_Y), ultimate tensile strength (σ_{UTS}), uniform elongation (el_{uni}) and total elongation (el_{Tot}) of the alloys at different processing conditions.

Alloy	Cooling rate (K s^{-1})	V_α (%)	σ_Y (MPa)	σ_{UTS} (MPa)	el_{uni} (± max 0.05 %)	el_{Tot} (± max 0.1%)
Ti-55511	10	46 ± 2	1102 ± 9	1142 ± 15	4.4	9.85
	1	54 ± 2	1141 ± 15	1189 ± 7	6.5	9.40
Ti-55521	10	34 ± 3	1031 ± 19	1091 ± 11	4.6	8.30
	1	41 ± 2	1053 ± 10	1116 ± 9	4.8	7.85

cooled at 1 K s^{-1} compared to those cooled at 10 K s^{-1} indicates β to α phase transformation. Ivasishin and Markovsky [64] have also mentioned that β to α phase transformation occurs during cooling in Ti alloys. The position of the β planes peaks shifts to the right resulting in smaller bcc lattice parameter. This is the effect of the presence of those alloying elements which have smaller atomic radii Al (143 pm), Mo (139 pm), V (134 pm), Cr (128 pm), and Fe (126 pm) compared to elemental Ti (147 pm). The same reason is mentioned in [56,57] for Ti–25V–15Cr–0.2Si and Ti–30Zr–5Al–3V alloys, respectively. As Ti-55521 alloy contains 1% more Cr, which has a much smaller atomic radius compared to elemental Ti, this results in an expected slightly smaller bcc lattice parameter than that for Ti-55511 alloy. On the other hand, hcp lattice parameters are not affected by the alloying elements because hcp phase contains α stabiliser Al (143 pm) as a main alloying element, which has a closer atomic radius to Ti (147 pm) compared to those of β stabilising alloying elements.

Under both cooling conditions, Ti-55521 alloy contains a smaller α crystallite size than Ti-55511 alloy. This is attributed to the slower rate of α phase transformation [37] caused by the presence of additional β-stabilising Cr and insufficient time for diffusion of β stabilisers out from the newly formed α. The restoration process after deformation (annihilation of dislocations, formation of dislocation cell structure) in α phase is found to be more advanced in the samples cooled at 1 K s^{-1}; as such samples remain a longer time at high temperatures compared to those cooled at 10 K s^{-1}. This, in turn results in less density of dislocations [34] and larger crystallite size of α in these specimens. Similar to the findings in [34], the β (110) plane has a higher dislocation density and microstrain compared to those of the α(10$\bar{1}$1) plane. There are two reasons for this observation: (i) the bcc crystal structure of β phase has more active slip systems than

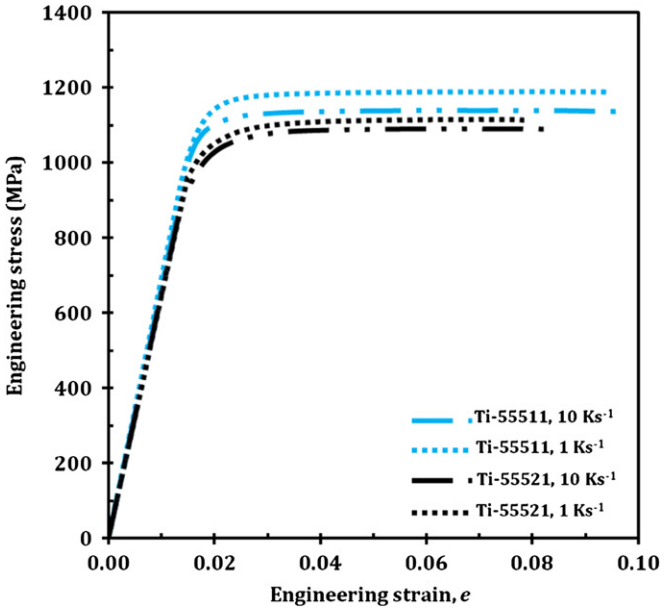

Fig. 6. The engineering stress versus engineering strain curves for both alloys under all cooling conditions.

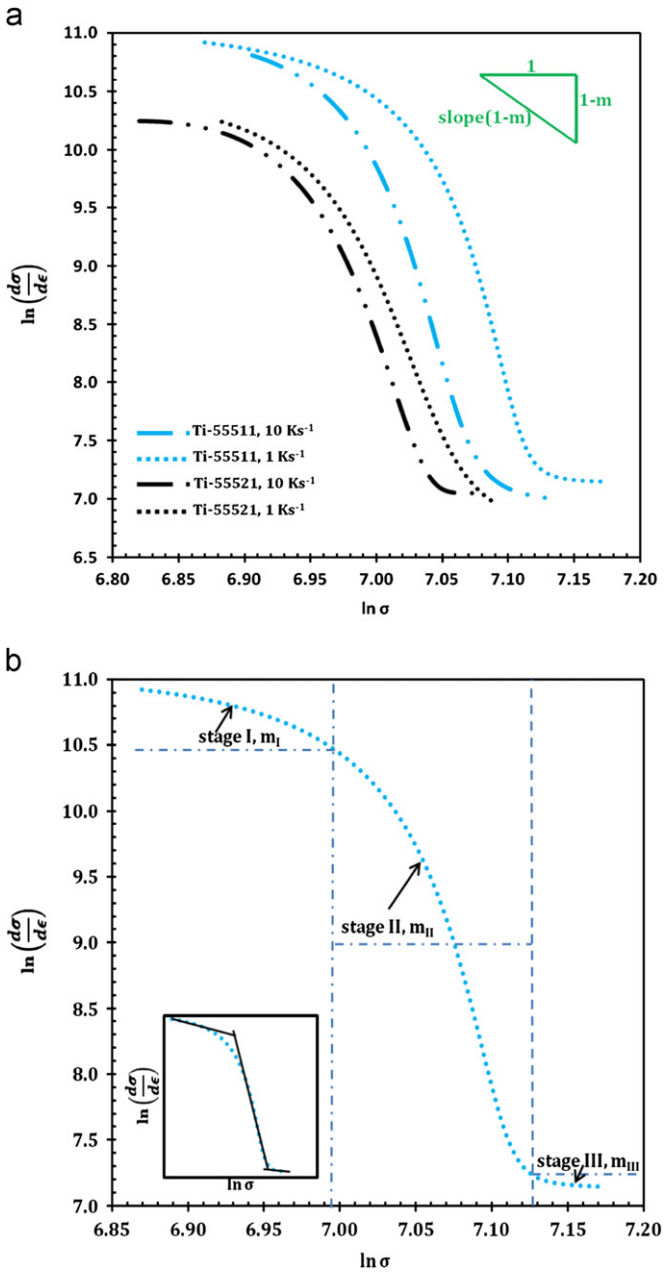

Fig. 7. (a) ln(dσ/dε) versus ln σ curves for both alloys under all cooling conditions where σ denotes true stress. (b) Representative illustration of ln(dσ/dε) versus ln σ curve for the Ti-55511 alloy cooled at 1 K s^{-1} showing three different work hardening stages (m_I, m_{II}, and m_{III}). The inset in (b) depicts the lines across the stages from where value for the slope (1−m) is obtained.

Table 5
The relationships between hardness, yield strength and volume fractions of phases present in the alloys.

Phase	VHN (H_v)	Calculated strength (MPa), $\sigma \approx H_v/3$	Alloy	Cooling rate (K s^{-1})	V_α (%)	Estimated 0.2% offset yield strength	Experimental 0.2% offset yield strength
α	434 ± 9	1416	Ti-55511	10	46 ± 2	1099 ± 12	1102 ± 9
β	253 ± 6	830		1	54 ± 2	1146 ± 12	1141 ± 15
α	431 ± 7	1409	Ti-55521	10	34 ± 3	1033 ± 17	1031 ± 19
β	257 ± 5	840		1	41 ± 2	1073 ± 11	1053 ± 10

Table 6
The value of work hardening exponent (m), transition true stress (σ_{tr}) and transition true strain (ε_{tr}) between the stages.

Alloy	Cooling rate (K s^{-1})	Stage I, m_{I}	Stage II, m_{II}	Stage III, m_{III}	$m_{\mathrm{I}} \rightarrow m_{\mathrm{II}}$		$m_{\mathrm{II}} \rightarrow m_{\mathrm{III}}$	
					σ_{tr} (MPa)	ε_{tr}	σ_{tr} (MPa)	ε_{tr}
Ti-55511	10	6.47	38.58	4.58	1092	0.018	1196	0.048
	1	9.56	45.72	5.91	1137	0.017	1240	0.045
Ti-55521	10	3.86	30.02	2.51	997	0.017	1139	0.046
	1	4.37	35.91	3.64	1016	0.016	1161	0.044

the hcp α phase. Thus, dislocation assisted slip activities during deformation at 1073 K occurs mostly in the β phase [65]. In addition, (ii) the remaining β phase is subjected to two deformations at 1173 K and 1073 K, whereas the α phase formed during holding at 1073 K is subjected only to single deformation (1073 K) and the α phase formed during cooling is not deformed. The increase in stored energy/dislocation density in the β planes at 1 K s^{-1} cooling rate could also be related to two concurrent phenomena taking place during cooling. Firstly, after the hot deformation at 1073 K, partial recrystallisation occurs in the remaining β phase [66] at high temperature during cooling. This results in the reduction of dislocation density. Recrystallisation of the whole remaining β phase is not completed due to the short time at high temperature during cooling. Secondly, the formation of a hard α phase inside the recrystallised β grains (Fig. 4e) during cooling has constrained the β phase resulting in high dislocation density at slower cooling than at faster cooling due to the higher volume fraction of α phase formed (Table 4). It appears that the second event plays a more dominant role, as a net effect is of a higher stored energy in slow cooled samples compared to that in the samples cooled at 10 K s^{-1}. A lower amount of α formed on cooling at 10 K s^{-1} due to a shorter time available results in less constrained β grains with lower stored energy.

4.2. Microstructural development

As a result of 60% deformation at 1073 K, globular shaped α phase is formed through breaking up of α lamellae, which formed previously during both cooling to and holding at 1073 K. Partial recrystallisation occurs during cooling of the heavily deformed (60%) β structure. It is more pronounced in the samples cooled at 1 K s^{-1} as more time is available. If multiple α phase crystals nucleate at the β grain boundaries in line, thereafter the grain boundary α is formed. It seems that during slower cooling (1 K s^{-1}), α phase nucleates preferably at β grain boundaries resulting in the presence of the interconnected grain boundary α (Fig. 4e). Sauer and Luetjering [67] have also mentioned that continuous α phase can be formed at β grain boundaries after cooling from the recrystallised temperature. The unusual phase transformation behaviour in Fig. 5 can be explained by observing the composition profile for the α and β phases, which shows that the newly formed α phase and the remaining inside β phase contain localised impurities, e.g. C and O. The higher concentrations of interstitial C and O are in α phase because they are α stabilisers, whereas the remaining β contains only traces of C and/or O. It could be proposed that due to the fast diffusion of interstitials C and O in the nuclei of α, the remaining β areas become more stable delaying the full transformation to α phase. On the other hand, the composition of the majority fully transformed α phase shows no O and/or C (Fig. 5aiii). This suggests that the areas showing unusual phase transformation behaviour (large bottom left corner in Fig. 5b) may have originally contained some oxide or carbide in the form of a surface layer on some powder particles [38].

Due to the addition of 1% more Cr in the Ti-55521 alloy less α phase is formed (Table 4) than in the Ti-55511 alloy, as this extra Cr content increases the Mo equivalent according to the following equation:

$$\mathrm{Mo}_{\mathrm{equivalent}} = 1 \times [\mathrm{Mo}] + 0.67 \times [\mathrm{V}] + 1.6 \times [\mathrm{Cr}] + 2.9 \times [\mathrm{Fe}] - 1 \times [\mathrm{Al}] \quad (8)$$

Weiss and Semiatin [68] have reported that the β-transus temperature decreases with increasing Mo equivalent. The 1% Cr has increased the Mo equivalent value to 9.45 for Ti-55521 alloy from 7.85 for Ti-55511 alloy. This difference in Mo equivalent reduces the β-transus temperature from ~1123 K [1] in the Ti-55511 alloy to ~1093 K for the Ti-55521 alloy [68]. Thus, the under cooling between the β-transus temperature and holding temperature of 1073 K is larger for the Ti-55511 alloy compared to that for the Ti-55521 alloy resulting in a higher volume fraction of α phase in Ti-55511 alloy. The similar results were obtained in [69] for Ti–10V–2Fe–3Al alloy where 50% of α volume fraction is formed by isothermal holding at 973 K for 1800 s and only 8.1% of α volume fraction is formed by isothermal holding at 1073 K for 1800 s. On the other hand, as the β to α phase transformation is a diffusion controlled transformation [64], the longer time available for transformation the higher volume fraction of the α phase formed. This is why for both alloys a larger volume fraction of α phase is obtained at relatively slower cooling rate of 1 K s^{-1} compared to that after 10 K s^{-1} cooling.

4.3. Mechanical properties

The strength of the alloy depends upon the properties and amounts of the phases present in the microstructure. Thus, the observed variation in strength could be explained by considering the changes in the volume fraction of α phase due to either processing difference (cooling rate) or compositional difference (wt% of Cr). Since α phase is harder than β phase, there is nearly a linear relationship between the strength and the amount of α phase (Table 5).

Although the amount of the α phase controls the strength of an alloy, its morphology affects the ductility. Terlinde et al. [21] have claimed that a change in shape from lamellae to globular of α phase increases the total elongation/ductility in Ti–10V–2Fe–3Al alloy. On the other hand, it has been reported that continuous networking nature of α phase deteriorates the total elongation/ductility [20,70,71]. In the present study, a reduction in total elongation is obtained for the samples cooled at 1 K s^{-1} cooling rate in both alloys, despite the presence of ~4% of globular-shaped α phase. This relatively low amount of the globular-shaped α may be insufficient to have a significant effect on the properties improvement, especially when the microstructures contain continuous and interconnected grain boundary α. Regardless of the cooling rate, the Ti-55521 alloy exhibited a lower total elongation compared to the Ti-55511 alloy. The possible reason for this is the

presence of more interconnected grain boundary α in the remaining β phase in Ti-55521 alloy compared to Ti-55511. This can be explained by the slower kinetics of α formation due to smaller under cooling below β transus, resulting in more free β grain boundaries available for α formation during cooling.

The modified C–J model has been applied to analyse the work hardening behaviour in the present study as it is generally used for two-phase materials [59–61]. It is mentioned in [61,62,72] that three stages in the work hardening behaviour depend upon the amount and type of the constituents present in the microstructure. Stage I corresponds to the plastic deformation of β phase that work hardens due to the glide of dislocations and formation of pile ups in the vicinity of the hard α phase grains which serve as barriers to dislocation motion and initially do not deform plastically. Consequently, strain gradient exists between the phases and within the β matrix. The higher the amount of α present, the more areas of high strain exist around α phase, and β phase work hardens faster, which corresponds to higher m_I. Stage II corresponds to the plastic deformation of soft β phase restrained between the hard α crystals, which continue to deform elastically. Stage III indicates the non-homogenous plastic deformation of both phases. The increase in m_I and m_{II} values with increasing the volume fraction of α in both alloys is in agreement with the literature [61,63,72], which also links the work hardening in the stage I with dislocation density, dislocation distribution and mobility of dislocations in the soft β phase.

5. Conclusions

The effects of final cooling rates, from 1073 K to room temperature, after TMP of two near-β Ti alloys on the microstructural parameters, phase transformation and mechanical properties were investigated. The following conclusions can be drawn:

- A β lattice distortion compared to unalloyed Ti is observed in both alloys and is attributed to the addition of the alloying elements. However, there is no effect of cooling rate on β lattice distortion. The α lattice parameters are unchanged in all experimental conditions.
- The slower final cooling results in a larger α crystallite sizes in both alloys, which is attributed to the annihilation of dislocations and formation of dislocation cell structure. Dislocation density is always found to be higher in the remaining β phase regardless of the cooling rates and alloy composition because (i) β phase is subjected to two high temperature deformations and (ii) ease of slip in the bcc crystal structure.
- The extent of β grain recrystallisation and continuous grain boundary α phase formation is more pronounced when the alloys are cooled slowly ($1\ K\ s^{-1}$). Both cooling rates and Cr content affect the volume fraction of α, which subsequently influences the strength of the studied alloys. Among all the samples, the Ti-55511 alloy cooled at $10\ K\ s^{-1}$ shows the highest total elongation with moderate UTS. For both alloys, slowly cooled samples showed a reduced total elongation. This is attributed to the formation of interconnected grain boundary α phase. The work hardening behaviour of the samples in all conditions is characterised by three distinct stages.

Acknowledgements

This work is funded by the Engineering Materials Institute strategic grant. The use of UOW Electron Microscopy Centre facilities, in particular JEOL 7001F, which was purchased with ARC support (LE0882613) is being acknowledged. The authors are grateful to Dr. A.A. Gazder for modification of tensile stage. One of the authors (Mansur Ahmed) would like to acknowledge the University Postgraduate Award (UPA) with International Postgraduate Tuition Award (IPTA) for his PhD study.

References

[1] O.M. Ivasishin, P.E. Markovsky, Yu.V. Matviychuk, S.L. Semiatin, C.H. Ward, S. Fox, J. Alloys Compd. 457 (2008) 296–309.
[2] O.M. Ivasishin, P.E. Markovsky, S.L. Semiatin, C.H. Ward, Mater. Sci. Eng. A 405 (2005) 296–305.
[3] O.M. Ivasishin, P.E. Markovsky, Yu.V. Matviychuk, S.L. Semiatin, Metall. Mater. Trans. A 34 (2003) 147–158.
[4] T. Saito, H. Takamiya, T. Furuta, Mater. Sci. Eng. A 243 (1998) 273–278.
[5] T. Saito, T. Furuta, Curr. Adv. Mater. Process., Iron Steel Inst. Jpn. 4 (1991) 1738–1739.
[6] F.H. Froes, D. Eylon, Int. Mater. Rev. 35 (1990) 162–184.
[7] M. Hagiwara, S. Emura, Mater. Sci. Eng. A 352 (2003) 85–92.
[8] K. Zhang, J. Mei, N. Wain, X. Wu, Metall. Mater. Trans. A 41 (2010) 1033–1045.
[9] W. Smarsly, Y.T. Lee, G. Welsch, Metall. Mater. Trans. A 16 (1985) 1831–1834.
[10] H. Jiang, K. Zhang, F.A. Garcia-Pastor, M.H. Loretto, D. Hu, P.J. Withers, M. Preuss, X. Wu, Mater. Sci. Technol. 27 (2011) 1241–1248.
[11] M.D. McNeese, D.C. Lagoudas, T.C. Pollock, Mater. Sci. Eng. A 280 (2010) 334–348.
[12] F.-C. Yen, K.-S. Hwang, Mater. Sci. Eng. A 528 (2011) 5296–5305.
[13] B. Ye, M.R. Matsen, D.C. Dunand, Acta Mater. 58 (2010) 3851–3859.
[14] V.A. Druz, V.S. Moxson, R. Chernenkoff, W.F. Jandeska Jr., J. Lynn, Met. Powder Rep. 61 (2006) 16–21.
[15] N. Zhang, P.B. Khosrovabadi, J.H. Lindenhovius, B.H Kolster, Mater. Sci. Eng. A 150 (1992) 263–270.
[16] J.C. Hey, A.P. Jardine, Mater. Sci. Eng. A 188 (1994) 291–300.
[17] D.G. Morris, M.A. Morris, Mater. Sci. Eng. A 110 (1989) 139–149.
[18] S.M. Green, D.M. Grant, N.R. Kelly, Powder Metall. 40 (1997) 43–47.
[19] O.M. Ivasishin, D. Eylon, V.I. Bondarchuk, D.G. Savvakin, Defect Diffusion Forum 277 (2008) 177–185.
[20] G.T. Terlinde, T.W. Duerig, J.C. Williams, Metall. Mater. Trans. A 14 (1983) 2101–2115.
[21] G. Terlinde, H.J. Rathjen, K.H. Schwalbe, Metall. Mater. Trans. A 19 (1988) 1037–1049.
[22] A Sarkar, A. Bhowmik, S. Suwas, Appl. Phys. A—Mater. Sci. Process. 94 (2009) 943–948.
[23] T. Ungár, M. Victoria, P. Marmy, P. Hanák, G. Szenes, J. Nucl. Mater. 276 (2000) 278–282.
[24] T. Shintani, Y. Murata, Acta Mater. 59 (2011) 4314–4322.
[25] X. Tian, Y. Zhang, Mater. Sci. Eng. A 516 (2009) 73–77.
[26] M.R. Movaghar Garabagh, S. Hossein Nedjad, H. Shirazi, M. Iranpour Mobarekeh, M. Nili Ahmadabadi, Thin Solid Films 516 (2008) 8117–8124.
[27] A Chanda, M. De, J. Alloys Compd. 313 (2000) 104–114.
[28] T. Ungar, H. Mughrabi, D. Rönnpagel, M. Wilkens, Acta Metall. 32 (1984) 333–342.
[29] F. Székely, I. Groma, J. Lendvai, Mater. Sci. Eng. A (309–310) (2001) 352–355.
[30] P.S. Chowdhury, A. Sarkar, P. Mukherjee, N. Gayathri, M. Bhattacharya, P. Barat, Mater. Charact. 61 (2010) 1061–1065.
[31] T. Ungár, O. Castelnau, G. Ribárik, M. Drakopoulos, J. Béchade, L.T. Chauveau, A. Snigirev, I. Snigireva, C. Schroer, B. Bacroix, Acta Mater. 55 (2007) 1117–1127.
[32] M.G. Glavicic, A.A. Salem, S.L. Semiatin, Acta Mater. 52 (2004) 647–655.
[33] M.G. Glavicic, S.L. Semiatin, Acta Mater. 54 (2006) 5337–5347.
[34] A Sarkar, S. Roy, S. Suwas, Mater. Charact. 62 (2011) 35–42.
[35] R. Boyer, R. Briggs, J. Mater. Eng. Perform. 14 (2005) 681–685.
[36] S. Banerjee, P. Mukhopadhyay, Phase Transformations: Examples from Titanium and Zirconium Alloys, Elsevier, Amsterdam, The Netherlands, 2007.
[37] M. Ahmed, A.A. Gazder, D.G. Savvakin, O.M. Ivasishin, E.V. Pereloma, J. Mater. Sci. 47 (2012) 7013–7025.
[38] A Carman, L.C. Zhang, O.M. Ivasishin, D.G. Savvakin, M.V. Matviychuk, E.V. Pereloma, Mater. Sci. Eng. A 528 (2011) 1686–1693.
[39] B.E. Warren, X-ray Diffraction, second ed., Courier Dover Publications, Mineola, NewYork, 1990.
[40] V. Randle, O. Engler, Introduction to Texture Analysis: Macrotexture, Microtexture and Orientation Mapping, second ed., CRC Press, Taylor & Francis Group, Boca Raton, FL, 2009.
[41] P. Scardi, M. Leoni, Acta Crystallogr. Sect. A 58 (2002) 190–200.
[42] D. Balzar, H. Ledbetter, J. Appl. Crystallogr. 26 (1993) 97–103.
[43] E.J. Mittemeijer, P. Scardi, Diffraction Analysis of the Microstructure of Materials, Springer, Berlin-Heidelberg, 2004.
[44] T. Ungár, A. Borbély, Appl. Phys. Lett. 69 (1996) 3173–3175.
[45] R.L. Snyder, H.J. Bunge, J. Fiala, Defect and Microstructure Analysis from Diffraction in International Union of Crystallography Monographs on Crystallography no. 10, 1999.
[46] L. Lutterotti, P. Scardi, J. Appl. Crystallogr. 23 (1990) 246–252.
[47] N. Popa, J. Appl. Crystallogr. 31 (1998) 176–180.
[48] W. Dollase, J. Appl. Crystallogr. 19 (1986) 267–272.
[49] R.E. Smallman, K.H. Westmacott, Philos. Mag. 2 (1957) 669–683.

[50] G.R. Stibitz, Phys. Rev. 49 (1936) 862–863.
[51] H. Ledbetter, H. Ogi, S. Kai, S. Kim, M. Hirao, J. Appl. Phys. 95 (2004) 4642–4644.
[52] A.N. Timoshevskii, S.O. Yablonovskii, O.M. Ivasishin, Funct. Mater. 19 (2012) 266–271.
[53] E.S. Fisher, M.H. Manghnani, J. Phys. Chem. Solids 32 (1971) 657–667.
[54] Y.T. Lee, M. Peters, G. Welsch, Metall. Mater. Trans. A 22 (1991) 709–714.
[55] B.D. Cullity, S.R. Stock, Elements of X-ray diffraction, third ed., Prentice Hall, Upper Saddle River, New Jersey, 2001.
[56] Y.Q. Zhao, S.W. Xin, W.D. Zeng, J. Alloys Compd. 481 (2009) 190–194.
[57] S.X. Liang, M.Z. Ma, R. Jing, Y.K. Zhou, Q. Jing, R.P. Liu, Mater. Sci. Eng. A 539 (2012) 42–47.
[58] H.M. Otte, A.L. Esquivel, Trans. Metall. Soc. AIME 233 (1965) 1276–1280.
[59] W. Nie, X. Wang, S. Wu, H. Guan, C. Shang, Sci. China Technol. Sci. 55 (2012) 1791–1796.
[60] A. Kumar, S.B. Singh, K.K. Ray, Mater. Sci. Eng. A 474 (2008) 270–282.
[61] F.H. Samuel, Mater. Sci. Eng. 92 (1987) L1–L4.
[62] A. Bag, K.K. Ray, E.S. Dwarakadasa, Metall. Mater. Trans. A 30 (1999) 1193–1202.
[63] H. Paruz, D.V. Edmonds, Mater. Sci. Eng. A 117 (1989) 67–74.
[64] O.M. Ivasishin, P.E. Markovsky, JOM 48 (1996) 48–52.
[65] M.K. Kumar, I. Samajdar, N. Venkatramani, G.K. Dey, R Tewari, D. Srivastava, S. Banerjee, Acta Mater. 51 (2003) 625–640.
[66] B.B. Rath, R.J. Lederich, C.F. Yolton, F.H. Froes, Metall. Mater. Trans. A 10 (1979) 1013–1019.
[67] C. Sauer, G. Luetjering, J Mater. Process. Technol. 117 (2001) 311–317.
[68] I. Weiss, S.L. Semiatin, Mater. Sci. Eng. A 243 (1998) 46–65.
[69] C. Li, X. Wu, J.H. Chen, S. van der Zwaag, Mater. Sci. Eng. A 528 (2011) 5854–5860.
[70] J. Chesnutt, F. Froes, Metall. Mater. Trans. A 8 (1977) 1013–1017.
[71] N. Clément, A. Lenain, P.J. Jacques, JOM 59 (2007) 50–53.
[72] R.A. Kot, B.L. Bramfitt, Fundamentals of dual-phase steels, in: Proceedings of the Symposium, Metallurgical Society of AIME, 1981.